Convective Stimulated Brillouin Scattering (SBS) in One- and Two-Ion Plasmas

Introduction

Stimulated brillouin scattering (SBS) is the decay of an incident (pump) light wave into a frequency-downshifted (Stokes) light wave and an ion-acoustic (sound) wave.[1] It is important in inertial confinement fusion (ICF) experiments because it scatters laser light away from the target, which reduces the laser energy that is available to drive the compression of the nuclear fuel.[2]

Unabated SBS results in a complete transfer of energy from the pump wave to the Stokes (and sound) wave(s); however, such a transfer is not observed in experiments. Several mechanisms can saturate SBS: The first and most important one is the Landau damping[3] of sound waves. This is a linear phenomenon and, hence, can be significant even for small sound-wave amplitudes. Heikkinen,[4] Rozmus,[5] and Cohen[6] have discussed a wide variety of ion-acoustic nonlinearities. Hydrodynamic effects such as daughter-wave generation and nonlinear phase shifts can limit SBS significantly if the sound-wave amplitude is large enough. Finally, if the Stokes intensity becomes comparable to the pump intensity, the effects of pump depletion become significant. Our goal is to compare these processes in one- and two-ion plasmas. Our model of sound waves consists of mass and momentum conservation equations for the ion fluids (two of each for two-ion plasmas), together with the inertionless electron-fluid equation and the Poisson equation. The results of kinetic theory[7–9] were used to calculate phenomenological damping coefficients. Beating the pump with Stokes waves creates a low-frequency ponderomotive force that drives the sound wave. In this article the exact partial differential equation for a light wave is not solved; instead, an approximate ordinary differential equation is used for the amplitude of the ponderomotive force. Neglecting the transient dynamics of the ponderomotive force is a good approximation because the group velocity of light is much higher than the group velocity of sound.

A one-dimensional model is used to simulate backward scattering. The first part of this article is devoted to SBS in a one-ion plasma. In this case it is easier to understand underlying physical processes and to find an approximate analytical solution of the model equations. A numerical solution was obtained by a code developed at LLE. To verify numerical results, the model equations were linearized, the exact dispersion equation was found, and it was solved numerically. The solution obtained through this method was compared to a numerical solution of linearized equations at different values of pump intensities and damping coefficients. The next step was to solve numerically the nonlinear equation for ponderomotive force along with the linear ion-fluid equation. That allowed us to quantify the effects of pump depletion. The latter solution was then compared to a solution of an exact nonlinear set of equations, which showed the effect of ion-acoustic nonlinearities. The same steps were repeated to simulate SBS in two-ion plasmas. The effects of Landau damping, pump depletion, and ion-acoustic nonlinearities are shown separately for fast and slow sound waves. SBS was simulated for carbon and hydrocarbon plasmas with parameters typical for experiments on the OMEGA laser system.

SBS in One-Ion Plasmas

1. Model Equations

The equations governing the ion-fluid motion are similar to the equations for undriven sound waves.[10] Specifically, each ion species is governed by a continuity equation

$$\partial_t n_i + \partial_x \left(n_i v_i \right) = 0 \tag{1}$$

and a momentum equation

$$m_i n_i \left(\partial_t + v_i \partial_x \right) v_i = -Ze\, n_i \partial_x \phi - \partial_x p_i, \tag{2}$$

where n_i is the ion (number) density, v_i is the ion velocity, m_i is the ion mass, Ze is the ion charge, p_i is the ion pressure, and ϕ is the electrostatic potential. One can use an adiabatic equation of state for ions under the assumption that the ion-acoustic wave phase velocity is much larger than the ion thermal velocity. It follows from the adiabatic equation of state

that

$$\partial_x p_i = 3n_{i0}T_i\left(n_i/n_{i0}\right)^2\partial_x\left(n_i/n_{i0}\right), \tag{3}$$

where T_{i0} is the equilibrium ion temperature and n_{i0} is the equilibrium ion density. By substituting Eq. (3) into Eq. (2), one finds that

$$m_i n_i\left(\partial_t + v_i\partial_x\right)v_i$$

$$= -Zen_i\partial_x\phi - 3n_{i0}T_{i0}\left(n_i/n_{i0}\right)^2\partial_x\left(n_i/n_{i0}\right). \tag{4}$$

The electrostatic potential is governed by the Poisson equation

$$\partial_{xx}\phi = 4\pi e\left(n_e - Zn_i\right). \tag{5}$$

With the ponderomotive term added,[1] the electron-fluid momentum equation is

$$\partial_t v_e = e\partial_x\phi/m_e - \partial_x\left(ea_\perp/m_e c\right)^2/2 - \partial_e p_e/n_e m_e, \tag{6}$$

where $a_\perp$ is the vector potential of a light wave. Because the electron thermal velocity is much higher than the phase velocity of the sound waves, one can use the isothermal equation of state

$$p_e = n_e T_e \tag{7}$$

for the electron fluid. By substituting Eq. (7) into Eq. (6) and neglecting electron inertia, one finds that

$$\partial_x n_e/n_e = e\partial_x\phi/T_e - e\partial_x d/T_e, \tag{8}$$

where the ponderomotive potential $d = a_\perp^2 e/2m_e c^2$. The integral of Eq. (8) is

$$n_e = n_{e0}\exp\left(e\phi/T_e - ed/T_e\right), \tag{9}$$

where n_{e0} is equilibrium electron density. One can simplify the manipulation of equations by rewriting them in dimensionless variables. It is clear from Eq. (9) that one should measure the potentials in units of T_e/e and the electron density in units of n_{e0}. It is clear from Eq. (4) that one should measure the ion density in units of n_{i0} (equilibrium ion density). It follows from Eq. (5) and the normalization of the potentials that one should measure distance (x) in units of the electron Debye length $\lambda_{\mathrm{De}} = \left(T_e/4\pi n_{e0}e^2\right)^{1/2}$. If one measures time ($t$) in units of the inverse ion-plasma frequency $\omega_{\mathrm{pi}}^{-1} = \left(m_i/4\pi Zn_{e0}e^2\right)^{1/2}$, the corresponding speed unit is the ion-sound speed $c_s = \left(ZT_e/m_i\right)^{1/2}$. By making these changes in Eqs. (1), (4), (5), and (9), one obtains the dimensionless equations

$$\partial_t N_i + \partial_x\left(N_i V_i\right) = 0, \tag{10}$$

$$\left(\partial_t + V_i\partial_x\right)V_i + \partial_x\Phi + \theta N_i\partial_x N_i = 0, \tag{11}$$

$$\partial_{xx}^2\Phi + N_i - N_e = 0, \tag{12}$$

$$N_e - \exp\left(\Phi - D\right) = 0, \tag{13}$$

where $\theta = 3T_i/ZT_e$. The dimensionless ponderomotive potential is given by

$$D = A_\perp^2, \tag{14}$$

where $A_\perp = ea_\perp/\left(2m_e T_e c^2\right)^{1/2}$ is the dimensionless vector potential of a light wave. Physically $A_\perp$ is the transverse electron quiver velocity divided by the electron thermal velocity. Equations (10)–(13) describe a sound wave in plasma. The equation for the vector potential of a light wave in a plasma was derived from the Maxwell equations:[1]

$$\left(\partial_{tt}^2 - c^2\partial_{xx}^2\right)A_\perp = -4\pi e^2 n_e A_\perp/m_e. \tag{15}$$

The vector potential $A_\perp$ can be written as

$$A_\perp = \left[A\exp\left(-i\omega_0 t\right) + \text{c.c.}\right]/2, \tag{16}$$

where A is the slowly varying amplitude and ω_0 is the pump frequency. Slowly varying amplitude A satisfies[5]

$$2i\left(n_c Z m_e / n_{e0} m_i\right)^{1/2} \partial_t A$$

$$+ c^2 m_e / T_e \partial_{xx}^2 A + n_c / n_{e0} a = A n_e / n_{e0}, \quad (17)$$

where $n_c = m_e \omega_0^2 / \left(4\pi e^2\right)$ is the critical density. The slowly varying amplitude can be expressed as the sum of two components:

$$A = A_0 \exp\left(ik_0 x\right) + A_1 \exp\left(ik_1 x - i\omega_1 t\right), \quad (18)$$

where $A_{0(1)}$ is the pump (Stokes)-wave amplitude, $k_{0(1)}$ is the pump (Stokes)-wave number, and ω_1 is the frequency difference between the pump and Stokes waves. If the SBS gain length is large compared to the wavelengths of pump and Stokes waves, the envelope approximation is valid. By substituting Eq. (18) into Eq. (17) and using envelope approximation, one finds that

$$\left(\partial_t A_0 / v_0 + \partial_x A_0\right) \exp\left(ik_0 x\right)$$

$$= -i\gamma A_1 \overline{N_e} \exp\left[i\left(k_1 + k_2\right)x - i\left(\omega_1 + \omega_2\right)t\right]/2, \quad (19)$$

$$\left(-\partial_t A_1^* / v_0 + \partial_x A_1^*\right) \exp\left(-ik_1 x + i\omega_1 t\right)$$

$$= -i\gamma A_0^* \overline{N_e} \exp\left[i\left(-k_0 + k_2\right)x - i\omega_2 t\right]/2, \quad (20)$$

where $\overline{N_e}$ is the first Fourier harmonic of the electron-density fluctuations, v_0 is the group velocity of the pump wave, $k_2(\omega_2)$ is the wave number (frequency) of the undriven sound wave, and the coupling constant $\gamma = T_e / \left(k_2 m_e c^2\right)$. In the context of SBS, the plasma response is important only near resonance. For three-wave processes the resonance conditions are

$$\omega_1 + \omega_2 = 0, \quad (21)$$

$$k_0 - k_1 - k_2 = 0. \quad (22)$$

The undriven sound-wave frequency ω_2 and wave number k_2 satisfy the dispersion relation[10]

$$\omega_2 = k_2\left[\left(1 + k_2^2\right) + \theta\right]^{1/2}. \quad (23)$$

By using Eqs. (21) and (22), one can reduce Eqs. (19) and (20) to

$$\partial_t A_0 / v_0 + \partial_x A_0 = -i\gamma A_1 \overline{N_e}/2, \quad (24)$$

$$-\partial_t A_1^* / v_0 + \partial_x A_1^* = -i\gamma A_0^* \overline{N_e}/2. \quad (25)$$

Because the light-wave group velocity is much higher than the sound-wave group velocity, the intrinsic relaxation time is much shorter than the SBS gain time. Consequently, the time derivatives in Eqs. (24) and (25) can be neglected, in which case the equations reduce to

$$\partial_x A_0 = -i\gamma A_1 \overline{N_e}/2, \quad (26)$$

$$\partial_x A_1^* = -i\gamma A_0^* \overline{N_e}/2. \quad (27)$$

By substituting Eq. (16) into Eq. (14) one finds that

$$D = \left[A^2 \exp\left(-2i\omega_0 t\right) + A^{*2} \exp\left(2i\omega_0 t\right) + 2|A|^2\right]/4. \quad (28)$$

The first two terms on the right-hand side of Eq. (28) are nonresonant and can be omitted, thus one obtains

$$D = |A|^2 / 2. \quad (29)$$

By substituting Eq. (18) into Eq. (29) and neglecting nonresonant terms, one finds that

$$D = \left[A_0 A_1^* \exp\left(ik_2 x - i\omega_2 t\right) + \text{c.c.}\right]/2. \quad (30)$$

It follows from Eq. (30) that the Fourier harmonic of the ponderomotive potential is

$$\overline{D} = A_0 A_1^*. \quad (31)$$

By differentiating Eq. (31) and substituting $\partial_x A_{0,1}$ from Eqs. (26) and (27), one obtains

$$\partial_x \overline{D} = -i\gamma \overline{N_e} \left(4\left|\overline{D}\right|^2 + C\right)^{1/2} \Big/ 2, \tag{32}$$

where the integration constant $C = \left(\left|A_0\right|^2 + \left|A_1\right|^2\right)^2 - 4\left|\overline{D}\right|^2$. One can calculate C at the left boundary ($x = 0$) and express it in terms of two physical parameters: the pump intensity $I = \left|A_0(0)\right|^2$ and the reflectivity $R = \left|A_1(0)\right|^2 \Big/ \left|A_0(0)\right|^2$:

$$C = \left[I(1-R)\right]^2. \tag{33}$$

The physical laser intensity $I_l = c\left(k_0\left|a_0\right|\right)^2 \Big/ (8\pi)$, from which it follows that the normalized intensity

$$I = \left(I_l e^2 \lambda_0^2\right) \Big/ \left(\pi m_e T_e c^3\right).$$

If I_l is measured in W/cm^2, λ_0 is measured in μm, and T_e is measured in keV, then

$$I \approx 2 \times 10^{-16}\, I_l \lambda_0^2 / T_e\,. \tag{34}$$

By adding phenomenological damping terms to Eqs. (11) and (12) and ponderomotive potential terms to Eqs. (13) and (14), one obtains

$$\partial_t N_i + \partial_x\left(N_i V_i\right) + \zeta\left(N_i - 1\right) = 0, \tag{35}$$

$$\left(\partial_t + V_i \partial_x\right) V_i + \partial_x \Phi + \theta N_i \partial_x N_i + \zeta V_i = 0, \tag{36}$$

$$\partial_{xx}^2 \Phi + N_i - \exp\left\{\Phi - \Re\left[\overline{D}\exp\left(ik_2 x - i\omega_2 t\right)\right]\right\} = 0, \tag{37}$$

$$N_e - \exp\left\{\Phi - \Re\left[\overline{D}\exp\left(ik_2 x - i\omega_2 t\right)\right]\right\} = 0, \tag{38}$$

where $\Re(f)$ denotes the real part of f. Equations (35)–(38), (32), and (33) form a complete set that self-consistently describes SBS.

We used the following initial and boundary conditions: the plasma is undisturbed initially and remains so at the left boundary ($x = 0$); SBS is seeded by a finite-amplitude Stokes wave at the right boundary ($x = L$). We used $\left|A_1(L)\right|^2 = 10^{-6} I$, which corresponds to

$$\left|\overline{D}(L)\right|^2 = 10^{-3} I. \tag{39}$$

2. Numerical Scheme

Our code uses the MacCormack (MC) method[11] to solve the ion-fluid Eqs. (35) and (36), written in conservation form. MC is a two-step method: at the first step the values of the ion density and velocity are predicted using the first-order forward difference scheme associated with Eqs. (35) and (36):

$$N_{ij}^{\overline{k+1}} = N_{ij}^k - c\left[\left(N_i V_i\right)_{j+1}^k - \left(N_i V_i\right)_j^k\right] - \delta t \zeta\left(N_{ij}^k - 1\right), \tag{40}$$

$$V_{ij}^{\overline{k+1}} = V_{ij}^k - c\left[\left(V_i^2/2 + \Phi + \theta N_i^2/2\right)_{j+1}^k - \left(V_i^2/2 + \Phi + \theta N_i^2/2\right)_j^k\right] - \delta t \zeta V_{ij}^k. \tag{41}$$

In Eqs. (40) and (41), the subscript j denotes the position $j\delta x$, the superscript k denotes the time $k\delta t$, and $c = \delta t/\delta x$ is the convection number.

With $N_{ij}^{\overline{k+1}}$ known, the predicted values of the electrostatic potential $\Phi_j^{\overline{k+1}}$, electron density $N_{ej}^{\overline{k+1}}$ and ponderomotive potential $D_j^{\overline{k+1}}$ can be determined by solving Eqs. (32), (33), (37), and (38) iteratively. First, Eq. (37) is solved using the ponderomotive potential obtained in the previous iteration (previous time step for the first iteration). Equation (37) is solved using the Newton iteration method, which was described in detail in Ref. 10. The values of the electrostatic potential obtained from Eq. (37) are used in Eq. (38) to calculate the electron density N_e. The discrete Fourier transform[12] is used to calculate the first harmonic of N_e. Fourier transform actually gives the values of the first harmonic averaged over one wavelength; thus, Eq. (32) has to be solved on a grid whose points are separated by exactly one wavelength. Linear interpolation was used to calculate the values of ponderomotive potential between those grid points:

$$\overline{D}(x) = \overline{D}\left(x_l\right) + \left[\overline{D}\left(x_r\right) - \overline{D}\left(x_l\right)\right]\left(x - x_1\right)/\lambda_2\,, \tag{42}$$

where x_l and x_r are left and right grid points and λ_2 is the sound wavelength. The square of the ponderomotive potential amplitude in Eq. (32) also has to be averaged over one wavelength: $\langle \overline{D}^2 \rangle = \int_{x_l}^{x_r} \overline{D}(x)^2 dx / \lambda_2$. By using formula (42) for $\overline{D}(x)$ and integrating, one obtains

$$\left\langle \overline{D}^2 \right\rangle = \left\{ \left|\overline{D}(x_l)\right|^2 + \left|\overline{D}(x_r)\right|^2 + \Re\left[\overline{D}(x_l)\right]\Re\left[\overline{D}(x_r)\right] + \Im\left[\overline{D}(x_l)\right]\Im\left[\overline{D}(x_r)\right] \right\} / 3, \tag{43}$$

where $\Im(f)$ denotes the imaginary part of f.

A straightforward numerical scheme is then used to solve Eq. (32):

$$\overline{D}_c(x_l) = \overline{D}_c(x_r) + i\gamma\lambda_2 \overline{N_e} \left(4\left\langle \overline{D}^2 \right\rangle_p + C \right)^{1/2} \Big/ 2. \tag{44}$$

The values of $\langle \overline{D}^2 \rangle_p$ and C_p obtained in the previous iteration (previous time step for the first iteration) are used to calculate $\overline{D}_c$ in the current iteration. The values of $\overline{D}_c$ are calculated from right to left because the value of $\overline{D}$ at the right boundary is fixed [Eq. (39)]. The values of $\overline{D}_c$ are then used in Eq. (33) to calculate R_c and C_c. Subsequently, Eq. (37) is solved using the values of ponderomotive potential obtained in the previous iteration. These iterations are repeated until the convergence condition

$$\left| \left(R_c - R_p \right) / R_p \right| < \epsilon \tag{45}$$

is satisfied. At the second step of the MC method, spatial derivatives are evaluated using the first-order forward-difference approximation based on the predicted values of the density, velocity, and electrostatic potential. Corrected values of density and velocity are obtained by averaging the spatial derivatives calculated at the first and second steps:

$$N_{i_j}^{k+1} = N_{i_j}^k - c\left[\left(N_i V_i\right)_{j+1}^k - \left(N_i V_i\right)_j^k + \left(N_i V_i\right)_j^{\overline{k+1}} - \left(N_i V_i\right)_{j-1}^{\overline{k+1}} \right] / 2 - \delta t \left[\xi\left(N_{i_j}^k - 1\right) + \xi\left(N_{i_j}^{\overline{k+1}} - 1\right) \right] / 2, \tag{46}$$

$$V_{i_j}^{k+1} = V_{i_j}^k - c\left[\left(V_i^2/2 + \Phi + \theta N_i^2/2\right)_{j+1}^k - \left(V_i^2/2 + \Phi + \theta N_i^2/2\right)_j^k + \left(V_i^2/2 + \Phi + \theta N_i^2/2\right)_j^{\overline{k+1}} - \left(V_i^2/2 + \Phi + \theta N_i^2/2\right)_{j-1}^{\overline{k+1}} \Big/ 2 - \delta t \left[\xi V_{i_j}^k + \xi V_{i_j}^{\overline{k+1}} \right] / 2. \tag{47}$$

The iterations described at the first step are repeated at the second step to calculate the corrected values of the electrostatic potential Φ_j^{k+1}, electron density N_{ej}^{k+1}, and ponderomotive potential amplitude $\overline{D}_j^{k+1}$. The MC method is of second-order accuracy in both time and space and is conditionally stable.[11] The Courant stability condition for the MC scheme applied to the sound-wave equations is derived in Ref. 10.

The sound-wave equations are solved on a spatial interval that is longer than the interaction length of the sound and light waves. To prevent the reflection of the sound wave from the right boundary, the spatial interval includes an extra region in which the sound wave is strongly damped and not driven.

3. Linear Regime of SBS

By linearizing Eqs. (35)–(38), one finds that

$$\partial_t N_i^{(1)} + \partial_x V_i^{(1)} + \xi N_i^{(1)} = 0, \tag{48}$$

$$\partial_t V_i^{(1)} + \partial_x \Phi + \theta \partial_x N_i^{(1)} + \xi V_i^{(1)} = 0, \tag{49}$$

$$\partial_{xx}^2 \Phi^{(1)} + N_i^{(1)} - N_e^{(1)} = 0, \tag{50}$$

$$N_e^{(1)} - \Phi^{(1)} + D^{(1)} = 0, \tag{51}$$

where $N_i^{(1)} = N_i - 1$, $N_e^{(1)} = N_e - 1$, $V_i^{(1)} = V_i$, $\Phi^{(1)} = \Phi$, and $D^{(1)} = D$. By substituting

$$y^{(1)} = \left[\tilde{y} \exp\left(-\sigma x + ik_2 x - i\omega_2 t\right) + \text{c.c.} \right],$$

where σ is the spatial growth rate, and differentiating, one obtains the linear equations

$$(i\omega - \zeta)\tilde{N}_i - (ik - \sigma)\tilde{V}_i = 0, \tag{52}$$

$$(i\omega - \zeta)\tilde{V}_i - (ik - \sigma)\left(\tilde{\Phi} + \theta\tilde{N}_i\right) = 0, \tag{53}$$

$$(ik - \sigma)^2\tilde{\Phi} + \tilde{N}_i - \tilde{N}_e = 0, \tag{54}$$

$$\tilde{N}_e - \tilde{\Phi} + \tilde{D} = 0, \tag{55}$$

in which ω and k are the frequency and wave number of the undriven sound wave (the subscript 2 was omitted for simplicity). By solving Eqs. (52)–(55) one finds that

$$\tilde{N}_e \Big/ (ik - \sigma)^2 = \left\{1 - 1\Big/\left[\theta(ik - \sigma)^2 - (i\omega - \zeta)^2\right]\right\}\left(\tilde{N}_e + \tilde{D}\right). \tag{56}$$

Linearization of the light-wave equation is equivalent to neglecting pump depletion

$$\partial_x \overline{D} = -i\gamma\, I\overline{N_e}/2. \tag{57}$$

One can rewrite Eq. (57) in terms of $\tilde{D} = \overline{D}\exp(-\sigma x)$ and $\tilde{N}_e = \overline{N}_e \exp(-\sigma x)$:

$$\tilde{D} = \tilde{N}_e i\gamma I/(2\sigma), \tag{58}$$

It follows from Eqs. (56) and (58) that

$$1/(ik - \sigma)^2 = \left\{1 - 1\Big/\left[\theta(ik - \sigma)^2 - (i\omega - \zeta)^2\right]\right\}\left[1 + i\gamma I/(2\sigma)\right]. \tag{59}$$

By using the sound-wave dispersion relation (23) and neglecting terms of second and higher order in σ/k and δ/ω, one can reduce Eq. (59) to

$$\sigma = -\gamma Ik/4\sigma + \eta\left(c_2\zeta - \theta\sigma\right), \tag{60}$$

where phase velocity $c_2 = \omega/k$ and $\eta = (1 + k^2)^2$. Equation (60) is a quadratic equation and can be solved analytically. The spatial growth rates are given by

$$\sigma_{\pm} = \frac{\eta c_2\zeta \pm \left[\eta^2 c_2^2\zeta^2 - \gamma Ik(1 + \eta\theta)\right]^{1/2}}{2(1 + \eta\theta)}. \tag{61}$$

By using boundary conditions for the ion density $N^{(1)}(0) = 0$, ponderomotive potential $D(L) = D_0 \cos(kx - \omega t)$, and Eq. (58), one finds that

$$D = D_0 \frac{\exp\left(-\sigma_+ x\right)/\sigma_+ - \exp\left(-\sigma_- x\right)/\sigma_-}{\exp\left(-\sigma_+ L\right)/\sigma_+ - \exp\left(-\sigma_- L\right)/\sigma_-} \times \cos\left(kx - \omega t\right), \tag{62}$$

$$N_i = 1 + 2D_0\left(1 + k^2\right)\frac{\exp\left(-\sigma_+ x\right) - \exp\left(-\sigma_- x\right)}{\exp\left(-\sigma_+ L\right)/\sigma_+ - \exp\left(-\sigma_- L\right)/\sigma_-} \times \sin\left(kx - \omega t\right)/(\gamma I). \tag{63}$$

Equation (60) has real solutions for growth rates σ only if

$$\zeta^2 > \gamma Ik(1 + \eta\theta)/(\eta c_2)^2. \tag{64}$$

When the ion-acoustic damping is weak, condition (64) is violated and there is no physically meaningful solution for σ. For this case the linear SBS equations predict absolute instability.[13] There is no steady-state solution of linear SBS equations in this case. The only saturation mechanisms in the case of weak ion-acoustic damping are nonlinear effects such as pump depletion and hydrodynamic nonlinearities. We consider convective SBS with strong ion-acoustic damping. In this case nonlinear effects can also be important, but even in the linear

regime SBS can be saturated by damping. For very strong damping

$$\zeta^2 >> \gamma Ik. \tag{65}$$

By neglecting the second- and higher-order powers of $\gamma Ik/\zeta^2$ in the Maclaurin expansion of formula (61), one obtains

$$\sigma_+ \approx \frac{\eta c_2 \zeta}{1+\eta\zeta} - \frac{\gamma Ik}{4\eta c_2 \zeta}, \tag{66}$$

$$\sigma_- \approx \frac{\gamma Ik}{4\eta c_2 \zeta}. \tag{67}$$

If condition (65) is satisfied, then $\sigma_+ >> \sigma_-$ and $\exp(-\sigma_+ x) << \exp(-\sigma_- x)$. Neglecting $\exp(-\sigma_+ x)$, one can reduce Eq. (62) to

$$D \approx D_0 \exp\left[G(L-x)\right] \cos\left(kx - \omega t\right), \tag{68}$$

where $G = \gamma Ik/4\eta c_2 \zeta$ is the well-known convective growth rate.

To assess the accuracy of the analytical approximations, we chose typical parameters and solved Eq. (59) numerically. There are up to eight solutions for σ, but only two of them have $\left|\Re(\sigma)\right| >> \left|\Im(\sigma)\right|$ and are relevant to SBS. For future reference we will refer to the solution obtained by the method described above as the combined solution.

We modeled SBS in a carbon plasma ($Z = 6$) with parameters that are typical of ICF experiments on the OMEGA laser system: $\lambda_0 = 0.35\ \mu$m, $I_L = 10^{15}$ W/cm^2, $T_e/T_i = 4$, $T_e = 1$ keV, and $n_{0e}/n_{cr} = 0.1$. We used kinetic theory[14] to evaluate the Landau damping rate

$$\zeta/\omega = \frac{(\pi/8)^{1/2}}{\left(1+k^2\right)} \times c_s \left[\left(\frac{m_e Z}{m_i}\right)^{1/2} + \left(\frac{T_e Z}{T_i}\right)^{3/2} \exp\left(-c_s^2 \frac{T_e Z}{2T_i}\right)\right]. \tag{69}$$

For the OMEGA parameters listed above, the Landau damping rate $\zeta/\omega \approx 3.5\%$.

The numerical (steady-state) solution of Eqs. (48)–(51) and (57) is compared to the analytical and combined solutions in Fig. 98.9. SBS in carbon plasma was simulated for the OMEGA-like parameters listed above. The three solutions agree perfectly. The reflectivity (R_N) obtained through direct numerical solution of Eqs. (48)–(51) and (57) = 20.6%. The reflectivity ($R_{A,C}$) obtained through analytical and combined solution = 20.8%. Relative difference $\left(R_{A,C} - R_N\right)/R_N = 0.9\%$.

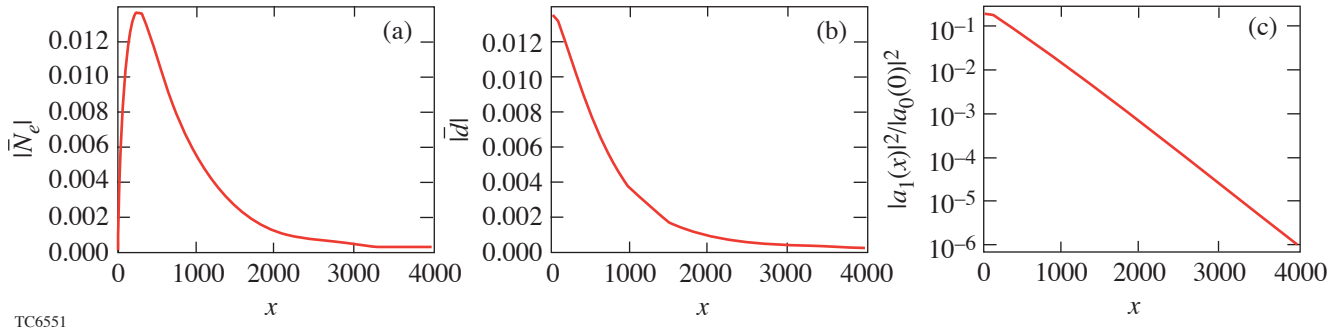

Figure 98.9
(a) First harmonic of electron density; (b) ponderomotive potential amplitude; (c) Stokes-wave intensity normalized to pump-wave intensity versus distance for steady state of SBS. Solutions of linearized equations [(48)–(51), (57)] describing SBS obtained through different methods are compared. Dotted lines represent numerical solution. Dashed lines represent combined solution obtained by numerical solution of Eq. (59). Solid lines represent analytical solution. All three solutions are indistinguishable. Simulation parameters are $\lambda_0 = 0.35\ \mu$m, $I_L = 10^{15}$ W/cm^2, $T_e/T_i = 4$, $T_e = 1$ keV, and $n_{0e}/n_{cr} = 0.1$.

4. Nonlinear Saturation

Convective SBS can be significantly reduced by nonlinear effects when the reflectivity is big enough. Pump depletion can be taken into account by solving the nonlinear light-wave equations (32) and (33). The effects of hydrodynamic nonlinearities can be determined by solving the nonlinear ion-fluid and Poisson equations (35)–(38). Different effects such as nonlinear phase shift[15] and generation of higher-order ion-wave harmonics of sound wave[4,5,16] were studied analytically. Our goal is to compare the effects of pump depletion and hydrodynamic nonlinearities on the saturation of SBS at OMEGA-like parameters. To separate the effects of pump depletion and hydrodynamic nonlinearities we numerically solved the nonlinear light-wave equations coupled with the linear sound-wave equations (48)–(51). This partially nonlinear solution was compared to the linear solution, based on Eqs. (48)–(51) and (57), and to the numerically obtained fully nonlinear solution, based on Eqs. (32), (33), and (35)–(38). All three solutions are shown in Figs. 98.10 and 98.11. Simulation parameters are the same as those used in the previous section.

Steady-state reflectivities are as follows: linear reflectivity $R_{LN} = 20.6\%$, partially nonlinear reflectivity $R_{PN} = 7.8\%$, fully nonlinear reflectivity $R_{FN} = 6.3\%$. Pump depletion reduces reflectivity by 60%. Ion-acoustic nonlinearities reduce reflectivity by 20%.

It is straightforward to express the pump intensity in terms of ponderomotive potential amplitude and constant of integration C. By using Eq. (31) and the definition of C, one finds that

$$|A_0|^2 = \left[\left(C + 4|\bar{D}|^2\right)^{1/2} + C^{1/2}\right]\Big/2. \qquad (70)$$

To show the effect of pump depletion we plotted the pump intensity based on the partially nonlinear solution. The pump-wave intensity normalized to the input pump intensity is shown as a function of distance in Fig. 98.12. The pump

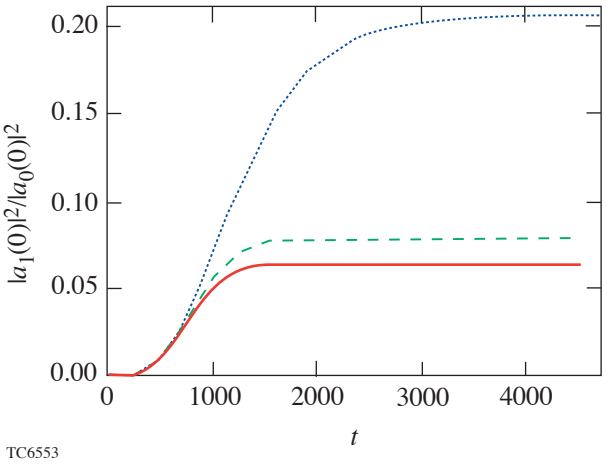

Figure 98.11
Reflectivities versus time. Dotted line represents numerical solution of linearized equations (48)–(51) and (57). Dashed line represents numerical solution of partially nonlinear equations (32), (33), and (48)–(51). Solid line represents numerical solution of fully nonlinear equations (32), (33), and (35)–(38). Simulation parameters are the same as in Fig. 98.9.

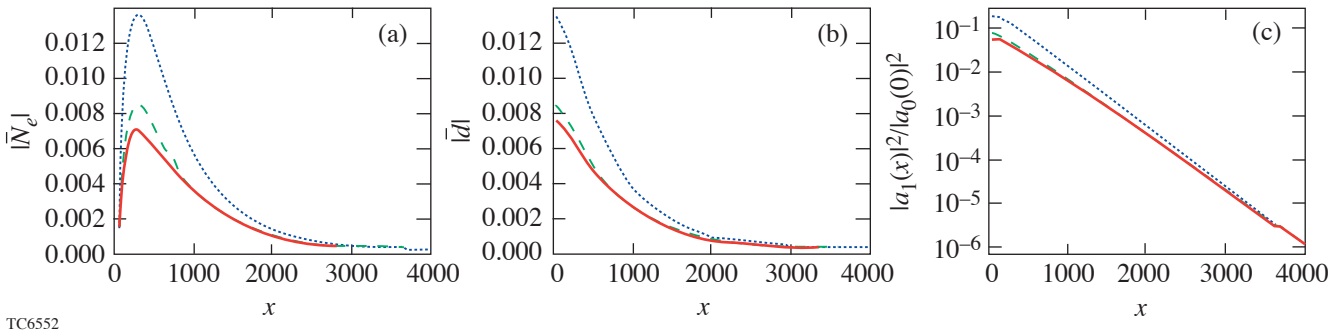

Figure 98.10
(a) First harmonic of electron density; (b) ponderomotive potential amplitude; (c) Stokes-wave intensity normalized to pump wave intensity versus distance for steady state of SBS. Dotted lines represent numerical solution of linearized equations (48)–(51) and (57). Dashed lines represent numerical solution of partially nonlinear equations (32), (33), and (48)–(51). Solid lines represent numerical solution of fully nonlinear equations (32), (33), and (35)–(38). Simulation parameters are the same as in Fig. 98.9.

intensity decreases on a scale length of several wavelengths. As one would expect, output pump intensity

$$|A_0(L)|^2 / I = 1 - R_{\mathrm{PN}} + |A_1(L)|^2 / I.$$

To show the higher-order harmonic generation, we plotted the discrete Fourier spectra of the electron density near its maximum. The absolute values of the harmonic amplitudes are shown in Fig. 98.13. The second and third harmonics can have significant amplitudes, whereas the fourth and higher harmonics are negligibly small.

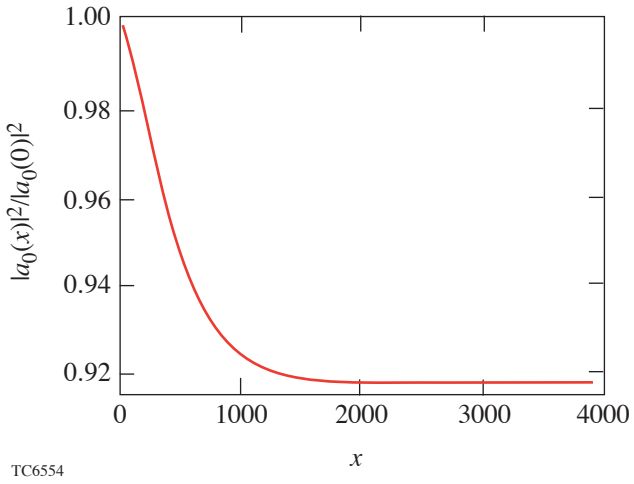

Figure 98.12
Pump-wave intensity normalized to input pump intensity versus distance for steady state of SBS. Simulation parameters are the same as in Fig. 98.9.

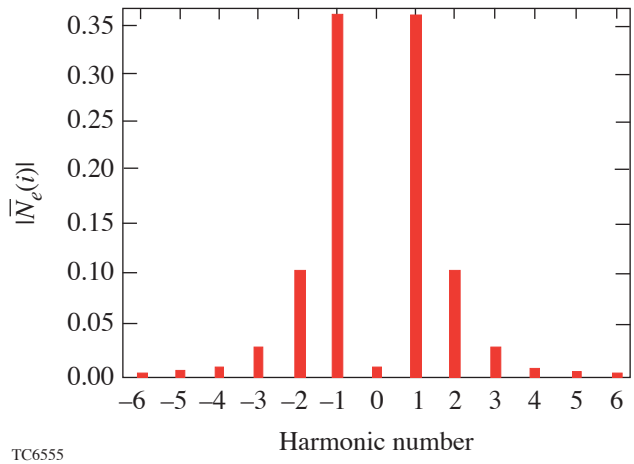

Figure 98.13
Fourier spectra of electron density near the point where it has maximal amplitude for steady state of SBS. Simulation parameters are the same as in Fig. 98.9.

SBS in Two-Ion Plasmas

1. Model Equations

The equations governing the ion-fluid motion are the same as those for undriven sound waves.[17] For each ion species s, the mass and momentum conservation equations are

$$\partial_t n_s + \partial_x \left(n_s v_s \right) = 0, \tag{71}$$

$$m_s n_s \left(\partial_t + v_s \partial_x \right) v_s + Z_s e n_s \partial_x \phi - \partial_x p_s = 0, \tag{72}$$

where n_s is the ion density, v_s is the ion velocity, m_s is the ion mass, $Z_s e$ is the ion charge, p_s is the ion pressure, and ϕ is the electrostatic potential. A detailed comparison of fluid and kinetic models of sound waves in two-ion plasmas is described in Ref. 9. In particular it shows that a fluid model with self-consistent values of adiabatic exponents approximates the kinetic phase velocities of the sound waves with an accuracy close to the accuracy of the fluid model with adiabatic exponents equal to 3 for both ion species. If one assumes adiabatic exponents equal to 3 for both ion species, one finds that

$$\partial_x p_s = 3 n_{s0} T_{s0} \left(n_s / n_{s0} \right)^2 \partial_x \left(n_s / n_{s0} \right), \tag{73}$$

where T_{s0} is the equilibrium ion temperature and n_{s0} is the equilibrium ion density. One can easily modify Eq. (73) for a polytropic equation of state. By substituting Eq. (73) into Eq. (72), one finds that

$$m_s n_s \left(\partial_t + v_s \partial_x \right) v_s$$

$$+ Z_s e n_s \partial_x \phi 3 n_{s0} T_{s0} \left(n_s / n_{s0} \right)^2 \partial_x \left(n_s / n_{s0} \right) = 0. \tag{74}$$

The evolution of the electrostatic potential is governed by the Poisson equation

$$\partial_{xx} \phi = 4\pi e \left(n_e - \sum_s Z_s n_s \right). \tag{75}$$

One can simplify the manipulation of these equations by normalizing n_s to n_{s0}, n_e to n_{e0}, and u_s to the sound speed of a reference species r. By rewriting Eqs. (71), (74), and (75) in the dimensionless form and adding phenomenological damping terms, one obtains

$$\partial_t N_s + \partial_x\left(N_s V_s\right) + \zeta\left(N_s - 1\right) = 0, \tag{76}$$

$$\left(\partial_t + V_s\partial_x\right)V_s + \beta_s\partial_x\Phi + \theta_s N_s\partial_x N_s + \zeta V_i = 0, \tag{77}$$

$$\partial_{xx}^2\Phi - N_e + \sum_s \alpha_s N_s = 0, \tag{78}$$

where $\theta_s = 3T_s/Z_r T_e\, m_r/m_s$, $\alpha_s = Z_s n_{s0}/n_{e0}$ is the ion charge-to-density ratio, and $\beta_s = Z_s m_r/Z_r m_s$ is the ion charge-to-mass ratio. Distance is measured in units of the electron-Debye length $\lambda_D = \left(T_e/4\pi e^2 n_{e0}\right)^{1/2}$, and time is measured in units of the reference ion-plasma period $1/\omega_{pi} = \left(m_r/4\pi Z_r e^2 n_{e0}\right)^{1/2}$. The equations for the electron density and ponderomotive potential amplitude are the same as those for the one-ion case: Eqs. (32), (33), and (38). We used the same initial and boundary conditions as in the one-ion case.

2. Numerical Scheme

A modified version of the numerical scheme described in the one-ion section was used to simulate SBS in two-ion plasmas. The mass- and momentum-conservation equations for each ion species are solved to evaluate the density N_s and velocity V_s of each of the ion fluids. Next, the Poisson equation (78) with a weighted sum of the light- and heavy-ion charge densities is used to calculate the electrostatic potential Φ. Equations (78), (33), (37), and (38) are solved using the iterative procedure described in the one-ion section. The Courant stability condition for the MC scheme applied to the sound-wave equation in two-ion plasmas is given in Ref. 17.

3. Linear Regime of SBS

By linearizing Eqs. (76)–(78), one finds that

$$\partial_t N_s^{(1)} + \partial_x V_s^{(1)} + \zeta N_s^{(1)} = 0, \tag{79}$$

$$\partial_t V_s^{(1)} + \beta_s\partial_x\Phi + \theta_s\partial_x N_s^{(1)} + \zeta V_s^{(1)} = 0, \tag{80}$$

$$\partial_{xx}^2\Phi^{(1)} + \sum_s \alpha_s N_s^{(1)} - N_e^{(1)} = 0. \tag{81}$$

By substituting $y^{(1)} = \left[\tilde{y}\exp\left(-\sigma x + ik_2 x - i\omega_2 t\right) - c.c.\right]$ into Eqs. (79)–(81) and differentiating, one obtains the linear algebraic equations

$$\left(i\omega - \zeta\right)\tilde{N}_s - \left(ik - \sigma\right)\tilde{V}_s = 0, \tag{82}$$

$$\left(i\omega - \zeta\right)\tilde{V}_s - \left(ik - \sigma\right)\beta_s\left(\tilde{\Phi} + \theta_s\tilde{N}_s\right) = 0, \tag{83}$$

$$\left(ik - \sigma\right)^2\tilde{\Phi} + \sum_s \alpha_s\tilde{N}_s - \tilde{N}_e = 0. \tag{84}$$

The undriven sound-wave frequency ω and wave number k satisfy the dispersion relation[17]

$$1 + k^2 = \sum_s \alpha_s\beta_s k^2\Big/\left(\omega^2 - \theta_s k^2\right). \tag{85}$$

The analysis of an undriven sound wave in two-ion plasmas was described in detail in Ref. 17. Two types of sound waves exist in such plasmas: a fast wave (fa), with phase speed in the range

$$c_{fa}^2 > \theta_l^2, \tag{86}$$

and a slow wave (sl), with phase speed in the range

$$\theta_h^2 < c_{sl}^2 < \theta_l^2, \tag{87}$$

where the indices l and h denote the lighter and heavier ions, respectively. Equation (85) is biquadratic and can be solved analytically. The frequencies are given by

$$\omega_{fa,sl}^2 = k^2\Big\{\mu_l + \theta_l^2 + \mu_h + \theta_h^2 \pm \left[\left(\mu_l + \theta_l^2 - \mu_h - \theta_h^2\right)^2 + 4\mu_l\mu_h\right]^{1/2}\Big\}\Big/2, \tag{88}$$

where $\mu_s = \alpha_s\beta_s/\left(1 + k^2\right)$. In Eq. (88) the plus sign is associated with the fast wave and the minus sign is associated with the slow wave. Both sound waves can be driven and participate in SBS. We artificially separated SBS from the fast and the slow sound waves by choosing the beat frequency of ponderomotive potential. Fast- or slow-wave SBS is modeled by driving the sound wave by ponderomotive potential, which has a corresponding frequency.

By combining Eqs. (82)–(84), (55), and (58), one finds that

$$1/(ik-\sigma)^2 = \left\{1-\sum_s \alpha_s\beta_s/\left[\theta_s(ik-\sigma)^2-(i\omega-\zeta)^2\right]\right\}\left[1+i\gamma I/(2\sigma)\right]. \quad (89)$$

As one should expect, the one-ion limit of Eq. (89) coincides with Eq. (59). Following the envelope-approximation procedure described in the one-ion section, we simplified Eq. (89) by substituting the undriven sound-wave frequencies given by Eq. (88) into Eq. (89) and neglecting second- and higher-order powers of σ/k and ζ/ω. The result is

$$\sigma = -\gamma Ik/4\sigma + \sum_s \alpha_s\beta_s\left(c_2\zeta-\theta_s\sigma\right)/\left(c_2^2-\theta_s\right)^2. \quad (90)$$

Equation (90) is quadratic and can be solved analytically. The growth rates are given by

$$\sigma_{1,2} = \frac{c_2\zeta\sum_s\chi_s}{2\left(1+\sum_s\chi_s\theta_s\right)} \pm \frac{\left[\left(c_2\zeta\sum_s\chi_s\right)^2-\gamma Ik\left(1+\sum_s\chi_s\theta_s\right)\right]^{1/2}}{2\left(1+\sum_s\chi_s\theta_s\right)}, \quad (91)$$

where $\chi_s = \alpha_s\beta_s/\left(c_2^2-\theta_s\right)^2$.

As in the one-ion case, this approximate analytical solution was compared to the exact numerical solution of Eq. (89). Just as in the one-ion case, there are up to eight numerical roots of Eq. (89), but only two of them have $|\Re(\sigma)| >> |\Im(\sigma)|$ and are relevant to SBS. The solution obtained by the numerical solution of the analytically derived equation for σ is also referred to as the combined solution.

The comparison of the approximate analytical solution to the exact numerical solution of Eq. (89) showed that in the case of a strong Landau damping $(\zeta/\omega \gtrsim 0.1)$, neglecting second-order powers of ζ/ω leads to a significant error in the growth-rate values.

We modeled SBS from fast and slow waves in hydrocarbon (CH) plasma (α_l = 1/7, α_h = 6/7, β_l = 1, β_h = 1/2), with parameters that are typical of ICF experiments on OMEGA: $\lambda_0 = 0.35$ μm, $I_L = 2\times10^{15}$ W/cm^2, $T_e/T_l = T_e/T_h = 4$, T_e = 1 keV, $n_{0e}/n_{cr} = 0.4$.

A detailed kinetic analysis of sound waves in two-ion plasmas is described in Refs. 7–9. We used the expression given in Ref. 9 for the Landau-damping rates:

$$\frac{\zeta_{fa(sl)}}{\omega_{fa(sl)}} = c_{fa(sl)}\frac{(\pi/8)^{1/2}}{1+\nu+k^2}\left[\left(\frac{m_eZ_r}{m_i}\right)^{1/2} + \sum_s \alpha_s\beta_s\left(\frac{3}{\theta_s}\right)^{3/2}\exp\left(-\frac{3c_{fa(sl)}^2}{2\theta_s}\right)\right], \quad (92)$$

where $\nu = 0$ for the fast wave and $\nu = 3\alpha_l/\theta_l$ for the slow wave. Coefficient ν reflects the reduction of the slow-wave damping rate by the light-ion Debye-screening factor. For the parameters listed above, the light-ion contribution to the Landau-damping rate (ζ_l) dominates for both fast and slow waves and $\zeta_l/\omega \approx 0.13$. The heavy-ion contribution for the fast wave is negligibly small $\left(\zeta_h/\omega \approx 10^{-6}\right)$ because the phase velocity of the fast wave is much closer to the thermal velocity of the light ions than to the thermal velocity of the heavy ions. The phase velocity of the slow wave lies between the thermal velocities of the light and heavy ions. For the stated parameters, the heavy-ion contribution to the slow-wave Landau-damping rate is significant $\left(\zeta_h/\omega \approx 0.013\right)$, but smaller than the light-ion contribution. The electron contribution (ζ_e) is significant for both waves. For the fast wave $\zeta_e/\omega \approx 0.01$, whereas for the slow wave $\zeta_e/\omega \approx 0.005$. The relative damping rates of fast and slow waves turn out to be close $\left(\zeta_{fa}/\omega_{fa} \approx 0.138,\ \zeta_{sl}/\omega_{sl} \approx 0.148\right)$. By definition the fast-wave frequency is higher than the slow-wave frequency, so the absolute damping rate of the fast wave, $\zeta_{fa} \approx 0.03$, is higher than the absolute damping rate of the slow wave, $\zeta_{sl} \approx 0.02$.

The combined solution, which was found by solving Eq. (89) numerically, was compared to the analytical solution of the envelope approximation of Eq. (89) and to the direct numerical stationary solution of Eqs. (79)–(81), (51), and (57). The numerical, combined, and analytical solutions of these equations are shown in Figs. 98.14 and 98.15 for fast- and slow-wave SBS, respectively. SBS in hydrocarbon plasma was simulated for the OMEGA-like parameters listed above. As in

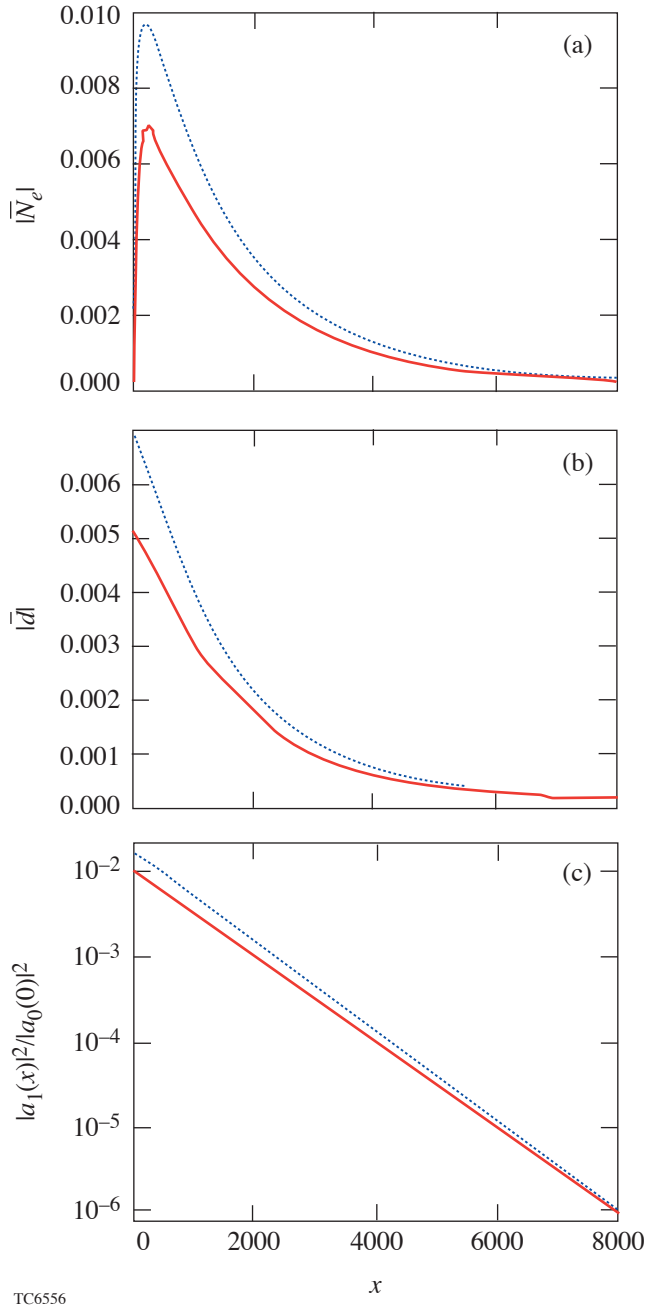

Figure 98.14
(a) First harmonic of electron density; (b) ponderomotive potential amplitude; (c) Stokes-wave intensity normalized to pump-wave intensity versus distance for steady state of fast-wave SBS. Solutions of linearized equations (51), (57), and (79)–(81) obtained through different methods are compared. Dotted lines represent numerical solution. Dashed lines represent combined solution obtained by numerical solution of Eq. (89). Solid lines represent analytical solution. Numerical and combined solutions are indistinguishable. Simulation parameters are $\lambda_0 = 0.35$ μm, $I_L = 2 \times 10^{15}$ W/cm^2, $T_e/T_l = T_e/T_h = 4$, $T_e = 1$ keV, and $n_{0e}/n_{cr} = 0.4$.

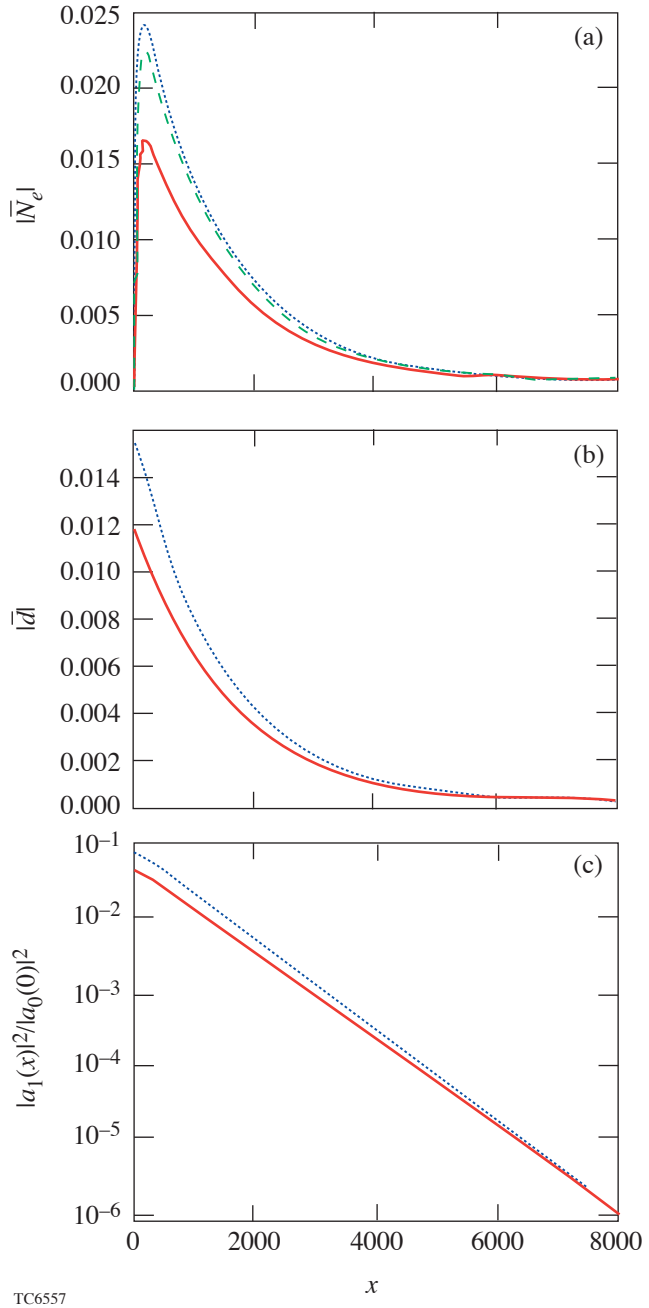

Figure 98.15
(a) First harmonic of electron density; (b) ponderomotive potential amplitude; (c) Stokes-wave intensity normalized to pump-wave intensity versus distance for steady state of slow-wave SBS. Solutions of linearized equations (51), (57), and (79)–(81) obtained through different methods are compared. Dotted lines represent numerical solution. Dashed lines represent combined solution obtained by numerical solution of Eq. (89). Solid lines represent analytical solution. Numerical and combined solutions for ponderomotive potential amplitude and Stokes-wave intensity are indistinguishable. Simulation parameters are the same as in Fig. 98.14.

the one-ion case, the numerical and combined solutions almost coincide. The fast-wave reflectivity obtained from the numerical solution is $R_N = 1.89\%$. The fast-wave reflectivity obtained from the combined solution is $R_C = 1.88\%$. The relative difference is $(R_C - R_N)/R_N = 0.2\%$. Fast-wave reflectivity obtained from the analytical solution is $R_A = 1.05\%$. The relative difference is $(R_A - R_N)/R_N = 44\%$. The slow-wave steady-state reflectivity obtained from the numerical solution is $R_N = 8.29\%$. The slow-wave reflectivity obtained from the combined solution is $R_C = 8.27\%$. The relative difference is $(R_C - R_N)/R_N = 0.25\%$. Slow-wave reflectivity obtained from the analytical solution is $R_A = 4.88\%$. The relative difference is $(R_A - R_N)/R_N = 41\%$. For both types of SBS the agreement between the numerical and combined solutions again proves the validity of the computational results. Landau-damping rates in CH plasmas are high for both fast and slow sound waves $(\zeta/\omega \simeq 0.14)$, which explains why analytical approximations are inaccurate in both cases. For the stated parameters, the Landau damping of the fast wave is stronger than that of the slow wave: $(\zeta_{fa} - \zeta_{sl})/\zeta_{sl} \approx 0.5$. The SBS growth rate is inversely proportional to the damping rate. This fact explains why the fast-wave SBS reflectivity is lower than the slow-wave SBS reflectivity: $R_{fa}/R_{sl} \approx 0.23$.

The first harmonics of the light- and heavy-ion densities ($\bar{N}_l$ and $\bar{N}_h$) in fast- and slow-wave SBS are shown in Figs. 98.16 and 98.17. Linear analysis of sound waves in two-ion plasmas shows that for fast wave $0 < \bar{N}_h/\bar{N}_l < 1$ and for

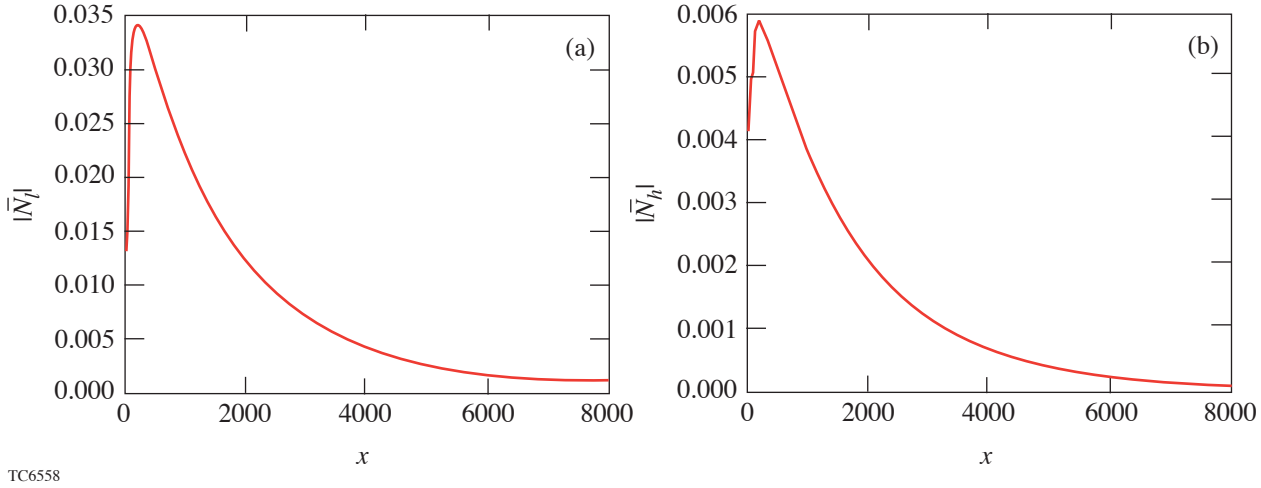

Figure 98.16
(a) First harmonic of light-ion and (b) heavy-ion densities versus distance for steady state of fast-wave SBS. Simulation parameters are the same as in Fig. 98.14.

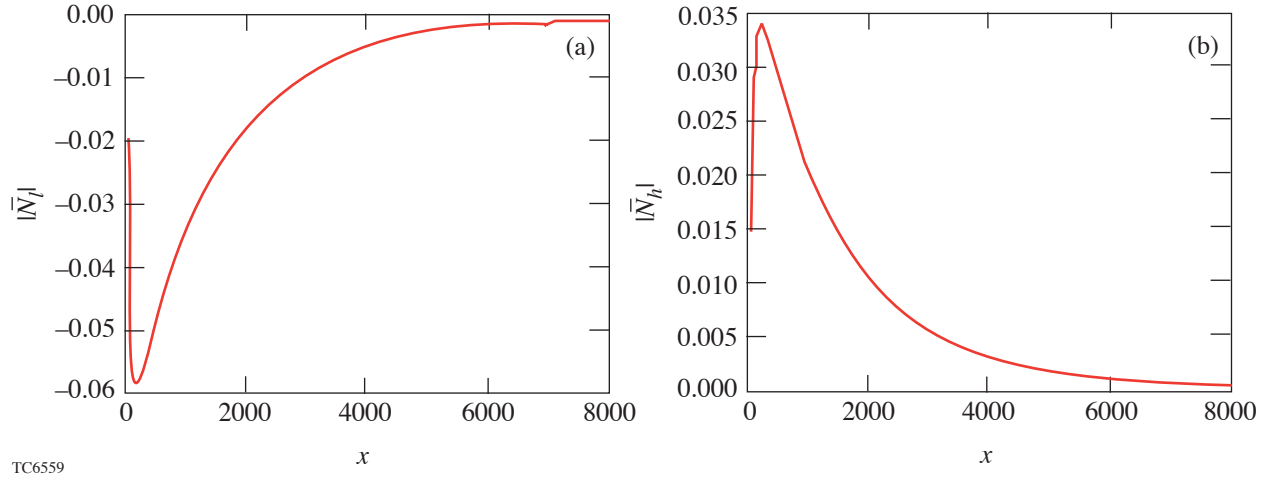

Figure 98.17
(a) First harmonic of light-ion and (b) heavy-ion densities versus distance for steady state of slow-wave SBS. Simulation parameters are the same as in Fig. 98.14.

slow wave $\overline{N}_h/\overline{N}_l < 0$.[17] Heavy ions are less mobile than light ions. Their density and velocity perturbations in the high-frequency field of the fast sound wave are smaller than the light-ion perturbations. The negative density ratio is a key feature of the slow sound wave. In the slow wave, light ions shield the electrostatic potential of the heavy ions and, hence, reduce the restoring force. The lower restoring force means lower frequency. At such low frequencies, heavy-ion perturbations are comparable to the light-ion perturbations.

4. Nonlinear Saturation

Figures 98.18–98.21 show the effects of hydrodynamic nonlinearities and pump depletion on the saturation of fast- and slow-wave SBS. The simulation parameters were listed in **Linear Regime of SBS** (p. 82). Similar to the one-ion case, the linear solution based on Eqs. (79)–(81), (51), and (57) was compared to the partially nonlinear solution based on Eqs. (79)–(81), (51), (32), and (33) and to the numerically obtained fully nonlinear solution, based on Eqs. (32), (33), and (76)–(78). This allowed us to separate the effects of hydrodynamic nonlinearities and pump depletion.

Steady-state reflectivities of fast-wave SBS are as follows: linear reflectivity $R_{LN} = 1.89\%$, partially nonlinear reflectivity $R_{PN} = 1.66\%$, and fully nonlinear reflectivity $R_{FN} = 1.6\%$. Pump depletion reduces reflectivity by 12%. Ion-acoustic nonlinearities reduce reflectivity by 3.8%.

Steady-state reflectivities of slow-wave SBS are as follows: linear reflectivity $R_{LN} = 8.29\%$, partially nonlinear reflectivity $R_{PN} = 5.09\%$, and fully nonlinear reflectivity $R_{FN} = 5.06\%$. Pump depletion reduces reflectivity by 39%. Ion-acoustic nonlinearities reduce reflectivity by 0.6%.

Nonlinear steepening of fast and slow sound waves was investigated in Ref. 17. In CH plasmas, the fast wave steepens much more than the slow wave. Wave steepening can be considered the generation of higher-order harmonics. Stronger steepening means that the amplitudes of the higher-order harmonics are bigger. These observations explain the difference in the effect of hydrodynamic nonlinearities on the saturation of fast- and slow-wave SBS. The reflectivity of slow-wave SBS is bigger than that of the fast-wave SBS. Consequently, the amplitude of the fast sound wave is smaller than that of the slow sound wave. On the other hand, if the fast- and slow-wave amplitudes were comparable, hydrodynamic nonlinearities would affect the fast-wave SBS much more than the slow-wave SBS. If the slow-wave reflectivity is much

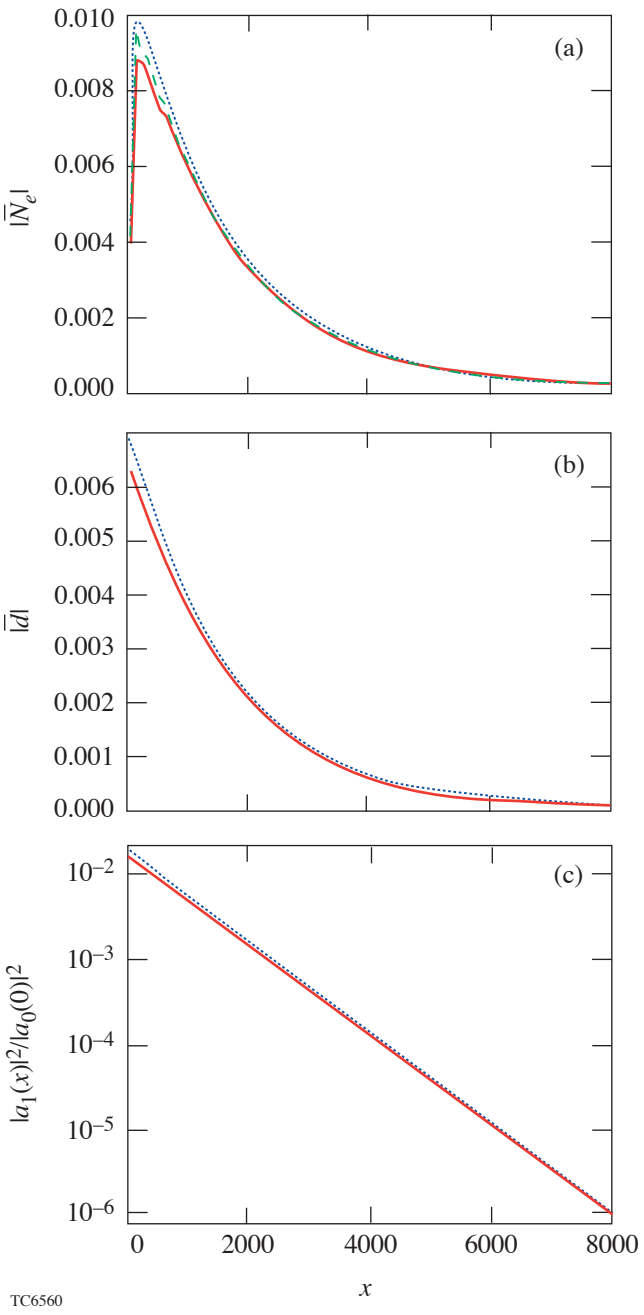

Figure 98.18
(a) First harmonic of electron density; (b) ponderomotive potential amplitude; (c) Stokes-wave intensity normalized to pump-wave intensity versus distance for steady state of fast-wave SBS. Dotted lines represent numerical solution of linearized equations (51), (57), and (79)–(81). Dashed lines represent numerical solution of partially nonlinear equations (32), (33), (51), and (79)–(81). Solid lines represent numerical solution of fully nonlinear equations (32), (33), and (76)–(78). Simulation parameters are the same as in Fig. 98.14.

higher than the fast-wave reflectivity, the slow-wave amplitude is much bigger than the fast-wave amplitude, in which case the effects of hydrodynamic nonlinearities can be more important for the slow wave than the fast wave. For the stated simulation parameters, the slow-wave reflectivity is not much higher than the fast-wave reflectivity $\left(R_{\mathrm{fa}} \approx 1\%,\ R_{\mathrm{sl}} \approx 5\%\right)$. In this case, hydrodynamic nonlinearities affect the fast-wave SBS more strongly than slow-wave SBS. Hydrodynamic nonlinearities reduce the fast-wave reflectivity by 3.8%, whereas they only reduce the slow-wave reflectivity by 0.6%

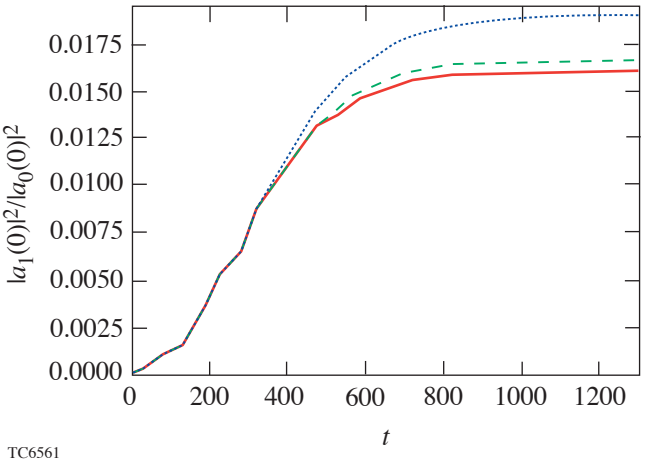

Figure 98.19
Reflectivities versus time for fast-wave SBS. Dotted lines represent numerical solution of linearized equations (51), (57), and (79)–(81). Dashed lines represent numerical solution of partially nonlinear equations (32), (33), (51), and (79)–(81). Solid lines represent numerical solution of fully nonlinear equations (32), (33), and (76)–(78). Simulation parameters are the same as in Fig. 98.14.

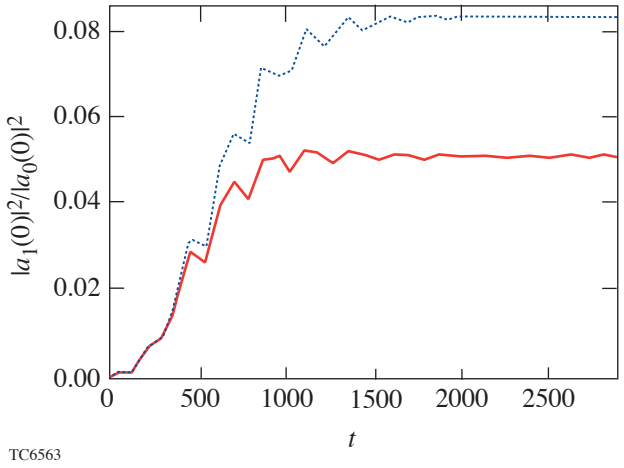

Figure 98.21
Reflectivities versus time for slow-wave SBS. Dotted lines represent numerical solution of linearized equations (51), (57), and (79)–(81). Dashed lines represent numerical solution of partially nonlinear equations (32), (33), (51), and (79)–(81). Solid lines represent numerical solution of fully nonlinear equations (32), (33), and (76)–(78). Simulation parameters are the same as in Fig. 98.14.

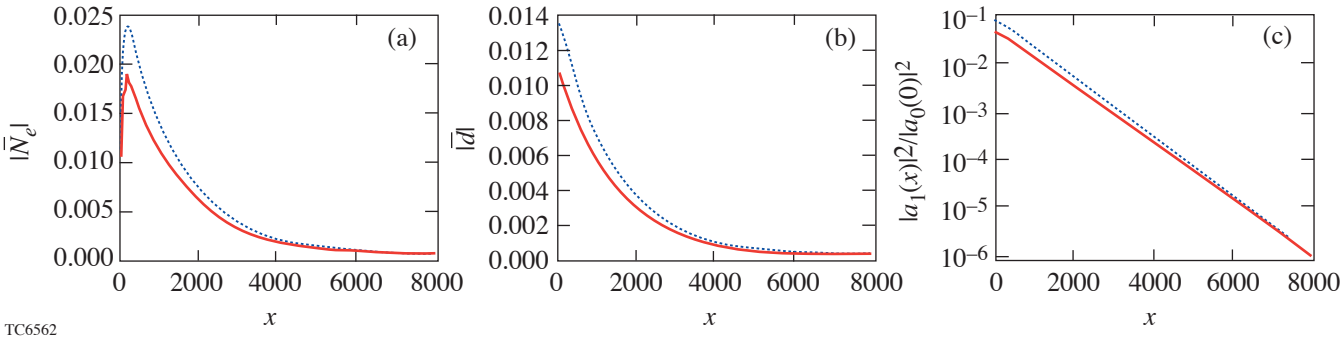

Figure 98.20
(a) First harmonic of electron density; (b) ponderomotive potential amplitude; (c) Stokes-wave intensity normalized to pump-wave intensity versus distance for steady state of slow-wave SBS. Dotted lines represent numerical solution of linearized equations (51), (57), and (79)–(81). Dashed lines represent numerical solution of partially nonlinear equations (32), (33), (51), and (79)–(81). Solid lines represent numerical solution of fully nonlinear equations (32), (33), and (76)–(78). Simulation parameters are the same as in Fig. 98.14.

The pump-wave intensities in fast- and slow-wave SBS are plotted as functions of distance in Figs. 98.22 and 98.23, respectively. Pump intensities are normalized to input pump intensity. The output pump intensity

$$\left|A_0(L)\right|^2 / I = 1 - R_{\mathrm{PN}} + \left|A_1(L)\right|^2 / I .$$

Light scattering by the slow sound wave decreases the pump intensity much more than scattering by the fast sound wave because the reflectivity of slow-wave SBS is higher than that of fast-wave SBS.

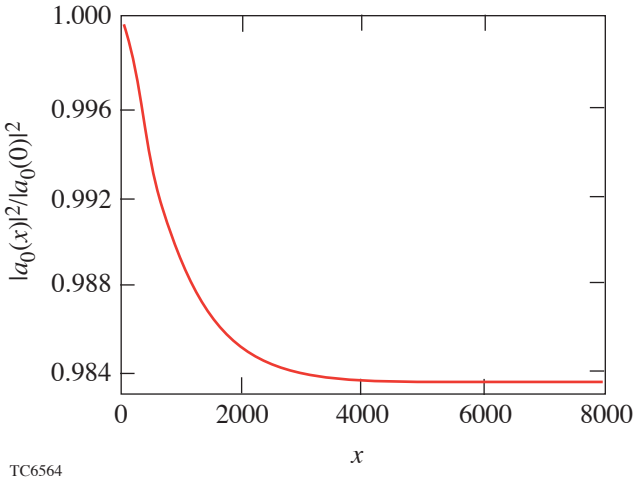

Figure 98.22
Pump-wave intensity normalized to input pump intensity versus distance for steady state of fast-wave SBS. Simulation parameters are the same as in Fig. 98.14.

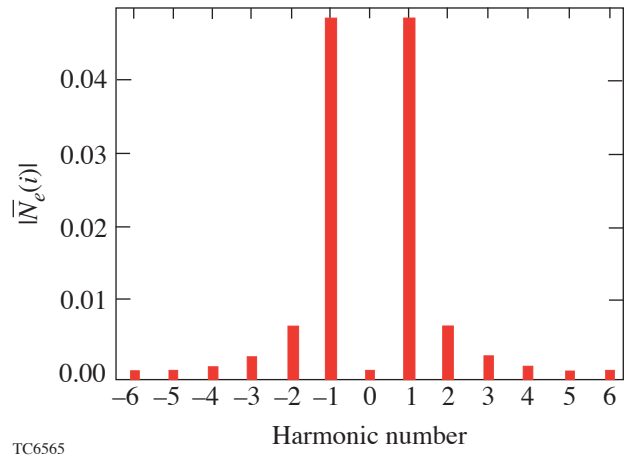

Figure 98.23
Fourier spectra of electron density near the point where it has maximal amplitude for steady state of fast-wave SBS. Simulation parameters are the same as in Fig. 98.14.

Higher-order harmonic generation is demonstrated by plotting discrete Fourier spectra of electron density near the point where it has maximal amplitude. The absolute values of the steady-state harmonics associated with the fast- and slow-wave SBS are shown in Figs. 98.24 and 98.25, respectively. The second- and higher-order harmonics are small in both the fast and slow sound waves because the amplitudes of both sound waves are small. The higher-order harmonics of fast-

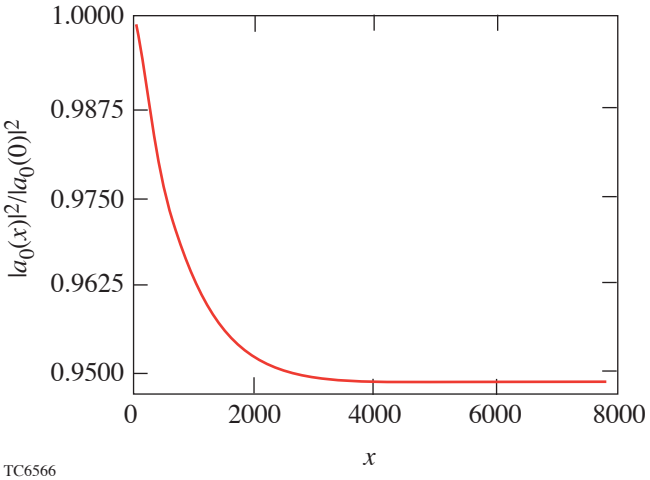

Figure 98.24
Pump-wave intensity normalized to input pump intensity versus distance for steady state of slow-wave SBS. Simulation parameters are the same as in Fig. 98.14.

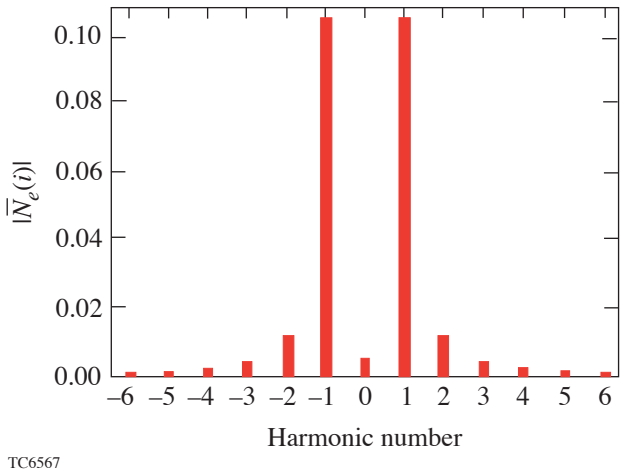

Figure 98.25
Fourier spectra of electron density near the point where it has maximal amplitude for steady state of slow-wave SBS. Simulation parameters are the same as in Fig. 98.14.

wave SBS are larger than the higher-order harmonics of slow-wave SBS because in CH plasmas the fast wave steepens much more than the slow wave. Consequently the effects of hydrodynamic nonlinearities on both the fast- and slow-wave SBS are small. They are noticeable for the fast-wave SBS but negligible for the slow-wave SBS.

Summary

A fluid model with phenomenological damping terms was used to study convective SBS in one- and two-ion plasmas. The Landau-damping rates were evaluated using formulas from kinetic theory. A fluid code was developed and tested by comparing its predictions to analytical formulas for SBS in the linear regime. SBS was simulated in carbon and hydrocarbon (CH) plasmas with OMEGA-like parameters. Two types of sound waves (fast and slow) exist in two-ion plasmas, each of which can participate in SBS. SBS from fast and slow sound waves were separated by choosing the beat frequency of the ponderomotive potential. The fast-wave reflectivity is lower than the slow-wave reflectivity because the Landau damping of the fast wave is stronger than the Landau damping of the slow wave. Effects of hydrodynamic nonlinearities and pump depletion on saturation of SBS in one- and two-ion plasmas were compared. The pump depletion significantly reduces reflectivity in one- and two-ion plasmas. The hydrodynamic nonlinearities are important for the SBS in one-ion carbon plasmas and noticeable for the fast-wave SBS in two-ion CH plasmas, but negligible for the slow-wave SBS.

Acknowledgment

The authors would like to thank D. D. Meyerhofer, W. Seka, J. Myatt, V. N. Goncharov, K. Vagin, I. Kuzora, and S. Urupin for fruitful discussions on this topic. This work was supported by the Department of Energy (DOE) Office of Inertial Confinement Fusion, under Cooperative Agreement No. DE-FC03-92SF19460, the University of Rochester, the New York State Research and Development Authority, and the Civilian Research and Development Foundation, under Award No. RP1-2268. The support of DOE does not constitute an endorsement by DOE of the views expressed in this article.

REFERENCES

1. W. L. Kruer, *The Physics of Laser-Plasma Interactions*, Frontiers in Physics, Vol. 73, edited by D. Pines (Addison-Wesley, Redwood City, CA, 1988), Chap. 4, pp. 37–43.

2. R. L. McCrory and J. M. Soures, in *Laser-Induced Plasmas and Applications*, edited by L. J. Radziemski and D. A. Cremers (Marcel Dekker, New York, 1989), pp. 207–268.

3. N. A. Krall and A. W. Trivelpiece, *Principles of Plasma Physics* (San Francisco Press, Inc., San Francisco, 1986).

4. J. A. Heikkinen, S. J. Karttunen, and R. R. E. Salomaa, Phys. Fluids **27**, 707 (1984).

5. W. Rozmus *et al.*, Phys. Fluids B **4**, 576 (1992).

6. B. I. Cohen *et al.*, Phys. Plasmas **4**, 956 (1997).

7. B. D. Fried, R. B. White, and T. K. Samec, Phys. Fluids **14**, 2388 (1971).

8. H. X. Vu, J. M. Wallace, and B. Bezzerides, Phys. Plasmas **1**, 3542 (1994).

9. E. A. Williams, R. L. Berger, R. P. Drake, A. M. Rubenchik, B. S. Bauer, D. D. Meyerhofer, A. C. Gaeris, and T. W. Johnston, Phys. Plasmas **2**, 129 (1995).

10. M. V. Kozlov and C. J. McKinstrie, Laboratory for Laser Energetics Report No. 321, NTIS document No. DOE/SF/19460-385, University of Rochester (2001). Copies may be obtained from the National Technical Information Service, Springfield, VA 22161.

11. J. D. Hoffman, *Numerical Methods for Engineers and Scientists* (McGraw-Hill, New York, 1992).

12. W. H. Press *et al.*, *Numerical Recipes in FORTRAN: The Art of Scientific Computing*, 2nd ed. (Cambridge University Press, Cambridge, England, 1992).

13. N. M. Kroll, J. Appl. Phys. **36**, 34 (1965); A. V. Maximov *et al.*, Phys. Plasmas **7**, 4227 (2000).

14. C. J. McKinstrie, R. E. Giacone, and E. A. Startsev, Phys. Plasmas **6**, 463 (1999).

15. V. V. Kurin and G. V. Permitin, Sov. J. Plasma Phys. **8**, 365 (1982).

16. S. J. Karttunen and R. R. E. Salomaa, Phys. Lett. A **72**, 336 (1979).

17. M. V. Kozlov and C. J. McKinstrie, Phys. Plasmas **9**, 3783 (2002).